Bull. Mater. Sci. (2024) 47:168
https://doi.org/10.1007/s12034-024-03236-x

Magnetic tunable thermal diffusivity of zinc ferrite/water nanofluid investigated using dual-beam thermal lens technique

M PIUS*, **F FRANCIS and S A JOSEPH**
Department of Physics and Centre for Research, St. Teresa's College (Autonomous), Ernakulam 682 011, India
*Author for correspondence (minupius@teresas.ac.in)

MS received 24 October 2023; accepted 13 February 2024

Abstract. In this study, we report how the zinc ferrite nanofluids constitute a great choice as heat transfer fluids due to their enhanced thermal diffusivity and magnetic tunability. The structure, morphology, magnetic and optical characteristics of nanoparticles in augmenting the thermal diffusivity were systematically analysed with a set of zinc ferrite nanoparticles synthesized at different calcination temperatures. Dual-beam thermal lens technique was then used to evaluate the thermal diffusivity of nanofluids, which demonstrated an increase of three times in thermal diffusivity than that of base fluid water. Subsequent experimental analysis performed in the presence of an external magnetic field revealed the magnetic tunability of thermal diffusivity for the first time with an estimated increase of six times than in the absence of a magnetic field. The optical imaging and field emission scanning electron microscopy of the nanofluid in the magnetic field supplemented the study in showing the significant effect of percolation due to the aggregate formation of nanoparticles being decisive in magnetic tunability of thermal diffusivity.

Keywords. Zinc ferrite nanoparticles; thermal diffusivity; magnetic tunability; dual-beam thermal lens method.

1. Introduction

Augmentation of heat transfer characteristics finds application in microelectronics, transportation, aerospace, condensers, solar collectors, automobile radiators, manufacturing, etc. [1,2]. The thermal conductivity of traditional heat transfer fluids, lubricants and coolants like water with inherently low thermal conductivity are reported to be enhanced with the trace addition of metals and metal oxides. Moreover, nanoparticles of metals suspended in liquid form nanofluids have shown superior features over micro-sized and milli-sized particles due to their stability and absence of clogging [3,4].

Prominent nanofluids of water, oil, ethylene glycol, etc., reported in the literature are formed by dissolving metallic nanoparticles, metal oxides, carbon-based structures like graphene and carbon nanotubes and polymers. Due to the interesting interactions and particle formations exhibited by water-based magnetic nanofluids in relation to the agglomeration processes, they are considered a special category of polar magnetic nanofluids. Thus, water-based magnetic nanofluids are considered as an excellent candidate for biomedical applications such as drug delivery, hyperthermia, magnetic field-mediated cell separation and contrast enhancement in magnetic resonance imaging [5]. Moreover, it could be controlled via adjusting the thermophysical properties such as thermal conductivity, thermal diffusivity and viscosity of the fluid or the thermo-magnetic convection current [6,7]. Size, distribution and morphology of dispersed magnetic particles, the stability and particle volume fraction of the nanofluid, and the chemical composition of magnetic particles are also significant factors affecting the thermal properties [8].

Among the different magnetic materials, the transition metal oxides like ferrites act as good candidates in the preparation of magnetic nanofluid owing to their high magnetocrystalline anisotropy, high coercivity, moderate saturation magnetization, good magnetostrictive coefficient, mono-disperse particle distribution and exceptional chemical stability. Due to its distinct tunable magneto-optic properties, effective energy transfer qualities, and mechanical and thermal stability, zinc ferrite ($ZnFe_2O_4$) has already become extremely important in a variety of applications [9,10]. All of the magnetic Fe^{3+} cations and nonmagnetic Zn^{2+} cations are positioned at tetrahedral (B) and octahedral (A) positions, respectively, in $ZnFe_2O_4$ with typical normal spinel structures [11]. According to reports, stoichiometry, synthesis pathways, digestion and calcination temperature, all play a significant role in adjusting the characteristics of zinc ferrite [12], hence making it a candidate for magnetic nanofluids. Several studies have been published on zinc ferrite nanofluids with improved thermal conductivity and heat transfer characteristics [13–18]. However, no studies have been published on the evaluation

Published online: 23 July 2024

of magnetic tunability of thermal diffusivity of $ZnFe_2O_4$ nanofluids.

There are only a few publications on the basic behaviour of thermal properties in the presence of magnetic fields and the measurement of other thermal parameters such as thermal diffusivity, despite the fact that extensive study has been done on determining the thermal conductivity of magnetic fluids. In comparison to studies on thermal conductivity, investigation of the thermal diffusivity of nanofluid can be done more quickly and with a smaller volume proportion. Additionally, compared to other traditional techniques like photoacoustic spectroscopy, laser flash technique, hotwire technique and photopyroelectric technique, the dual-beam thermal lens technique is more sensitive in determining the thermal diffusivity. The technique measures thermal lens formation based on the little differences in refractive index across the beam width brought on by very slight temperature variations in liquids. The benefits of this method include high sensitivity as it measures optical energy directly absorbed, its applicability with even a small volume of the sample and its dependence on solvent thermo-optical characteristics [19–21].

The work thus projects the estimation of the thermal diffusivity of zinc ferrite as nanofluid using the thermal lens dual-beam spectroscopic technique in the presence of the external magnetic field. The work also elucidates the calcination temperature-dependent properties of zinc ferrite nanoparticles which are dispersed in deionized water by ultrasonic agitation to form magnetic nanofluid. The thermal diffusivity of magnetic nanofluid is evaluated at various particle volume fractions with the application of the external magnetic field and compared with the case when no magnetic field is applied.

2. Experimental

2.1 *Materials*

Zinc (II) chloride ($ZnCl_2$) ($\geq$ 98%), iron (III) chloride hexahydrate ($FeCl_3\ 6H_2O$) ($\geq$ 98%) and sodium hydroxide pellets (NaOH) ($\geq$ 97%) employed for the synthesis were purchased from Sigma Aldrich and used without further purification.

2.2 *Synthesis*

Zinc ferrite nanoparticles were synthesized via co-precipitation method from chloride precursors, taken in the stoichiometric ratio of 2:1, and NaOH as precipitating agent. A detailed explanation of the synthesis is given elsewhere [18] in our earlier publication. The samples are referred to as ZF100 to ZF800 based on the calcination temperatures, the precipitates are subjected to, i.e., from 100 to 800°C, respectively.

2.3 *Characterization*

X-ray diffraction (XRD), obtained via Bruker AXS D8 Advance X-ray diffractometer employing Cu-Kα radiation of wavelength 1.54 Å, was used to study the crystallinity of synthesized samples. Field emission scanning electron microscopic (FESEM) images obtained using ZEISS SIGMA HV04-93 confirmed the morphology and composition of the samples. Optical properties were examined by the analysis of Ultraviolet–Visible Diffusive Reflectance spectra (UV-VIS DRS), recorded using Perkin Elmer lambda 950 UV-VIS-NIR instrument in 200–1200 nm range. Photoluminescence studies were conducted using Shimadzu RF 6000 spectrofluorophotometer. Room temperature magnetization studies of samples were performed using a Vibrating Sample Magnetometer Lake Shore VSM 7410 with -15 kOe $<$ H $<$ 15 kOe as an applied field. Coherent Sapphire SF 488 nm 50 mW as pump beam and Coherent Radius 640 nm 25 mW as probe beam were employed for dual-beam thermal lens spectroscopic analysis. The magnetic field was established using pair of neodymium magnets.

2.4 *Dual-beam thermal lens method*

The thermal diffusivity of the synthesized sample was estimated using thermal lens spectroscopy as explained in reports [14,18]. The nanofluids of synthesized samples were prepared in water with a concentration of 1 g l^{-1}. The fluid contained in a sample cell was placed near the focal plane and pumped with a laser beam (488 nm) matching the absorbance of the sample. The variation in refractive index constituted a thermal lens in the medium, which depended on the rise time of the excitation pump pulse and the thermal time constant of the medium. As a consequence, when the probe laser of 640 nm (wavelength away from the absorption edge) passes through this path, it gets expanded, and the corresponding fall in intensity of the beam was monitored. The change in probe beam intensity $I(t)$ with time t with the formation of thermal lens due to the passage of pump beam was monitored and fitted theoretically using equation (1) to estimate the time constant (t_c) for thermal lens formation. The thermal diffusivity (D) of the sample is hence calculated using equation (2), where the parameter θ is related to radiated thermal power (P_{th}), laser wavelength (λ_L), thermal conductivity (k), temperature-dependent refractive index gradient (dn/dT) given by equation (3). The same set up was used to analyse the magnetic tunability of the thermal diffusivity except that a pair of magnets were placed alongside the sample cell to set up the external magnetic field perpendicular to the beam passage. The schematic representation of the experimental set up is shown in figure 1.

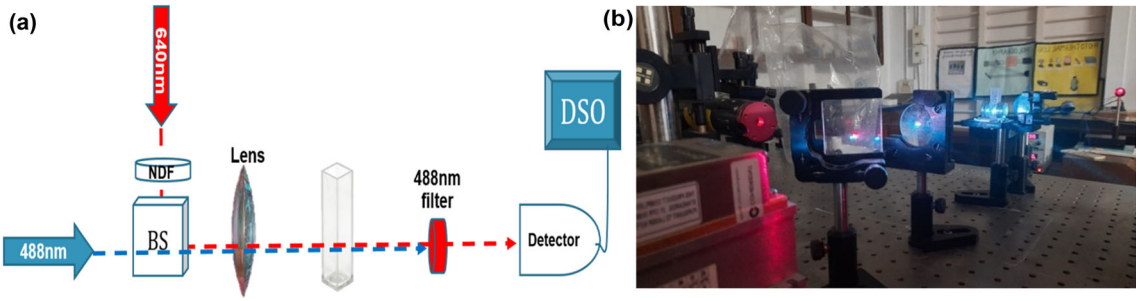

Figure 1. (**a**) Schematic set of dual-beam thermal lens technique. (**b**) Experimental set up in the laboratory.

$$I(t) = I_0\left[1 - \frac{\theta}{\left(1+\frac{t_c}{2t}\right)} + \frac{\theta^2}{2\left(1+\frac{t_c}{2t}\right)^2}\right]^{-1}. \quad (1)$$

$$D = \frac{\omega^2}{4t_c}. \quad (2)$$

$$\theta = \frac{P_{th}\left(\frac{dn}{dT}\right)}{\lambda_L k}. \quad (3)$$

3. Results and discussion

3.1 *X-ray diffraction studies*

The formation of the cubic lattice of the spinel phase of zinc ferrite nanoparticles with Fd-3m (227) space group was confirmed in the samples calcined at 400°C and above in our earlier publication [18]. The high intensity and distinct peaks in the XRD pattern seen for high-temperature calcined samples verified the increase in crystallinity with temperature, which were described as being caused by the rapid grain development and agglomeration.

Further in the present study, the lattice parameter (a) and crystallite size (D_c) were calculated for the differently calcined samples using equation (4) for the cubic lattice and Debye Scherrer formula [22], given by equation (5), from the most intense peak (311) in the XRD pattern, respectively. The crystallite size was also calculated using the Cauchy equation given by equation (6). The slope and intercept value from Williamson–Hall plot drawn between $\beta\cos\theta$ (y-axis) and $4\sin\theta$ (x-axis) as in figure 2 give the microstrain (ε) and crystallite size (0.89 λ/intercept), respectively.

The samples' positive strain indicates tensile strain that is linked to lattice expansion. Additionally, it was discovered that the size of the crystallites and the lattice strain increased with the calcination temperature, which may result from the coalescence of grain boundaries and smaller grains [23]. The origins of the strain may also include stacking faults, contact or sinter stresses, lattice dislocations, etc.

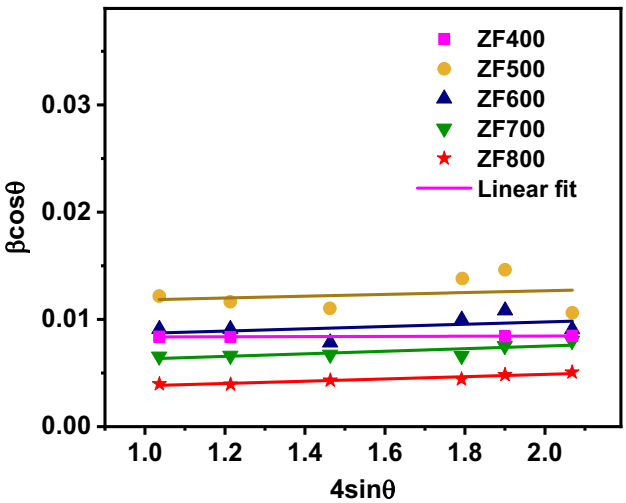

Figure 2. W–H plot of zinc ferrite ZF400, ZF500, ZF600, ZF700 and ZF800 nanoparticles.

$$a = d\sqrt{h^2 + k^2 + l^2}. \quad (4)$$

$$D_c = \frac{0.9\lambda}{\beta\cos\theta} \quad (5)$$

$$\beta\cos\theta = \frac{0.89\lambda}{D_c} + 4\varepsilon\sin\theta \quad (6)$$

The values tabulated in table 1 show that a smaller crystallite size was obtained using the Scherrer method than the other methods, as it does not account for the induced strain and the instrumental factors affecting the broadening.

3.2 *Fourier transform infrared studies*

According to Fourier transform infrared (FTIR) measurements, the distinctive peaks of spinel ferrite, which are due to the vibrations of metal-oxide in octahedral and tetrahedral voids, began to appear at calcination temperatures above 400°C as shown in figure 3a. The peaks at 533 and 400 cm^{-1}, respectively, demonstrate the Zn–O vibration in tetrahedral (A) sites and the Fe–O vibration in octahedral (B) sites. The shoulder bands found close to these bands for ZF700 and ZF800 can be attributed to the presence of

Table 1. Crystallite size, lattice strain and spacing, grain size and bandgap of zinc ferrite nanoparticles calcined at 400, 500, 600, 700 and 800°C.

Sample	Crystallite size (nm)			Lattice strain 10^{-4}	Lattice parameter [Å] (std 8.44)	Grain size (FESEM) (nm)	Bandgap (eV)
	Debye Scherer (311)	W–H plot	Cauchy equation				
ZF400	16	17	17	8.48	8.418	18	2.013
ZF500	12	12	13	8.47	8.420	16	1.967
ZF600	15	18	17	9.63	8.412	18	2.102
ZF700	22	27	26	12.0	8.417	29	2.122
ZF800	35	50	56	12.6	8.414	44	2.150

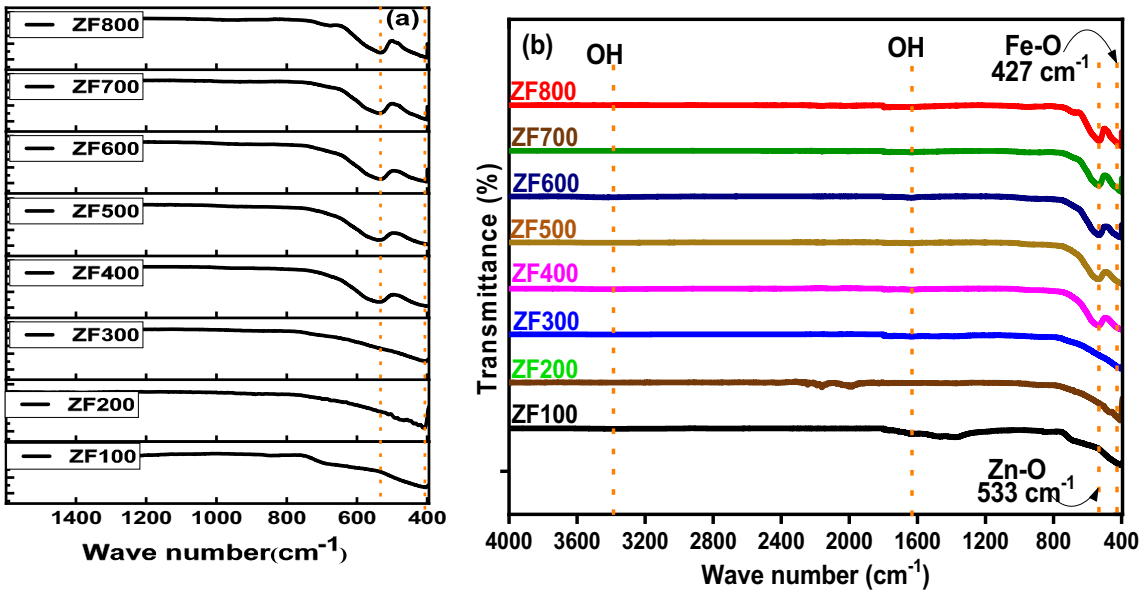

Figure 3. (**a**) FTIR spectra of ZF100–ZF800 in the range 4000–400 cm^{-1}. (**b**) Formation of two metal oxide characteristic peaks of spinel ferrite with calcination temperature.

cations with different ionic states both in octahedral and tetrahedral sites and the corresponding encroachment of Zn^{2+} ions to the B-site and subsequent migration of Fe^{3+} ions to the A-site [24]. It is also seen in figure 3b that the absorbance due to stretching and bending vibration of adsorbed water molecules assigned in the frequencies around 3400 and 1600 cm^{-1}, respectively, have significantly decreased with increased calcination temperature.

3.3 *Morphological studies*

The morphology of the samples assessed using the FESEM (figure 4) showed a non-uniform aggregate of spherical grains in low-temperature calcined samples, while the uniformity and particle size increased with calcination temperature. The crystallite size matched the particle size in high-temperature cases which supports the single-domain formation, which will be explained in Section 3.6.

3.4 *UV–VIS diffuse reflectance spectroscopic analysis*

The DRS spectrum showed four prominent reductions in reflectance (i.e., absorption bands) in the regions from 220 to 380 nm, 380 to 670 nm, 670 to 950 nm and 950 to 1200 nm, as shown in figure 5a. These can be related to the ligand field transitions due to the electron excitation from t_{2g} into e_g orbitals, formed by the splitting of the 3d orbitals in the presence of the electrical field of nearby O^{2-} anions, and the transitions caused by ligands-to-metal charge transfer. The direct transition $O^{2-} + Fe^{3+} \rightarrow O^{-} + Fe^{2+}$ causes a dip in reflectance observed at 630 nm. An

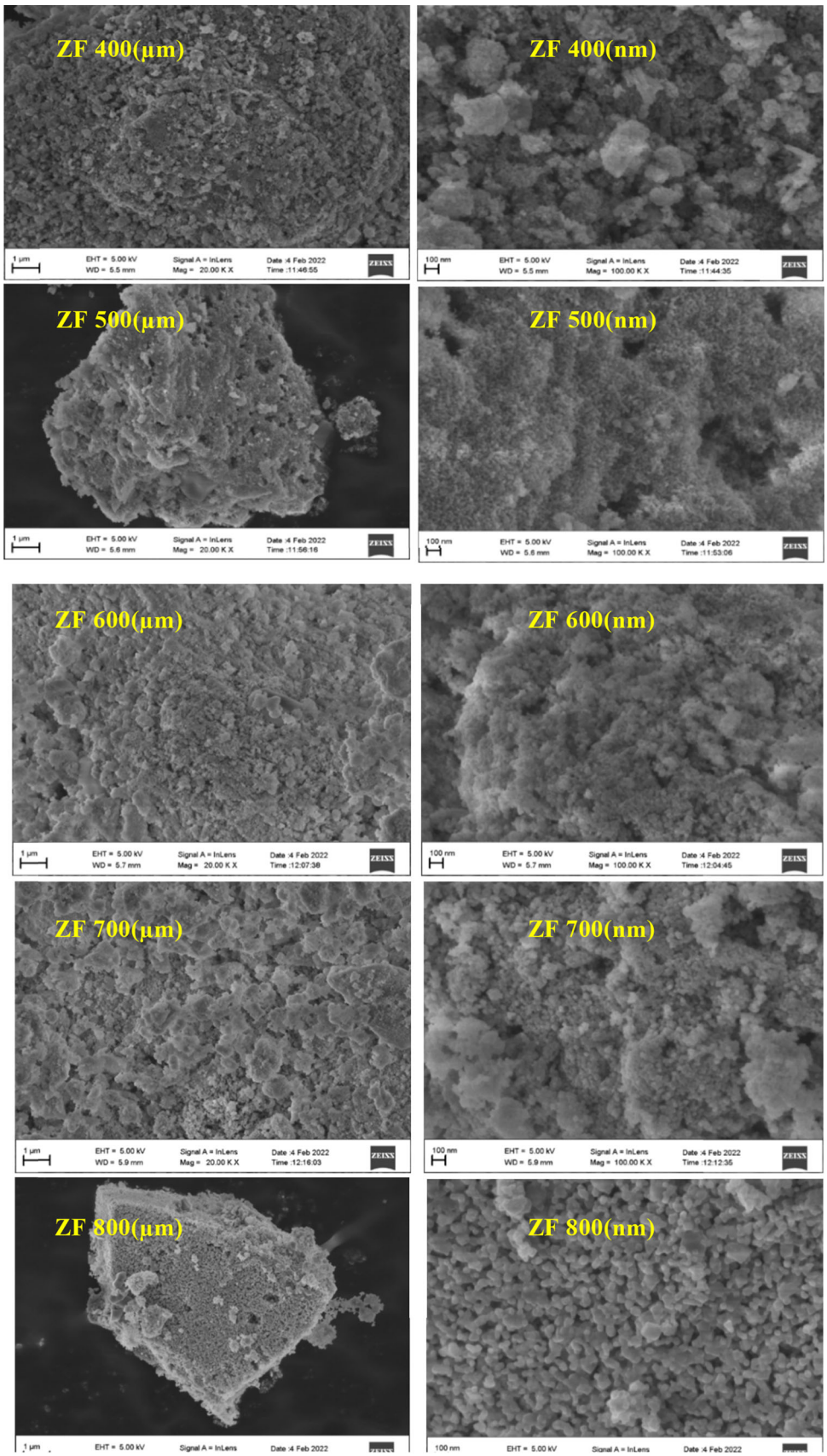

Figure 4. Microstructures of ZF400, ZF500, ZF600, ZF700 and ZF800 nanoparticles in micrometre and nanometre scales.

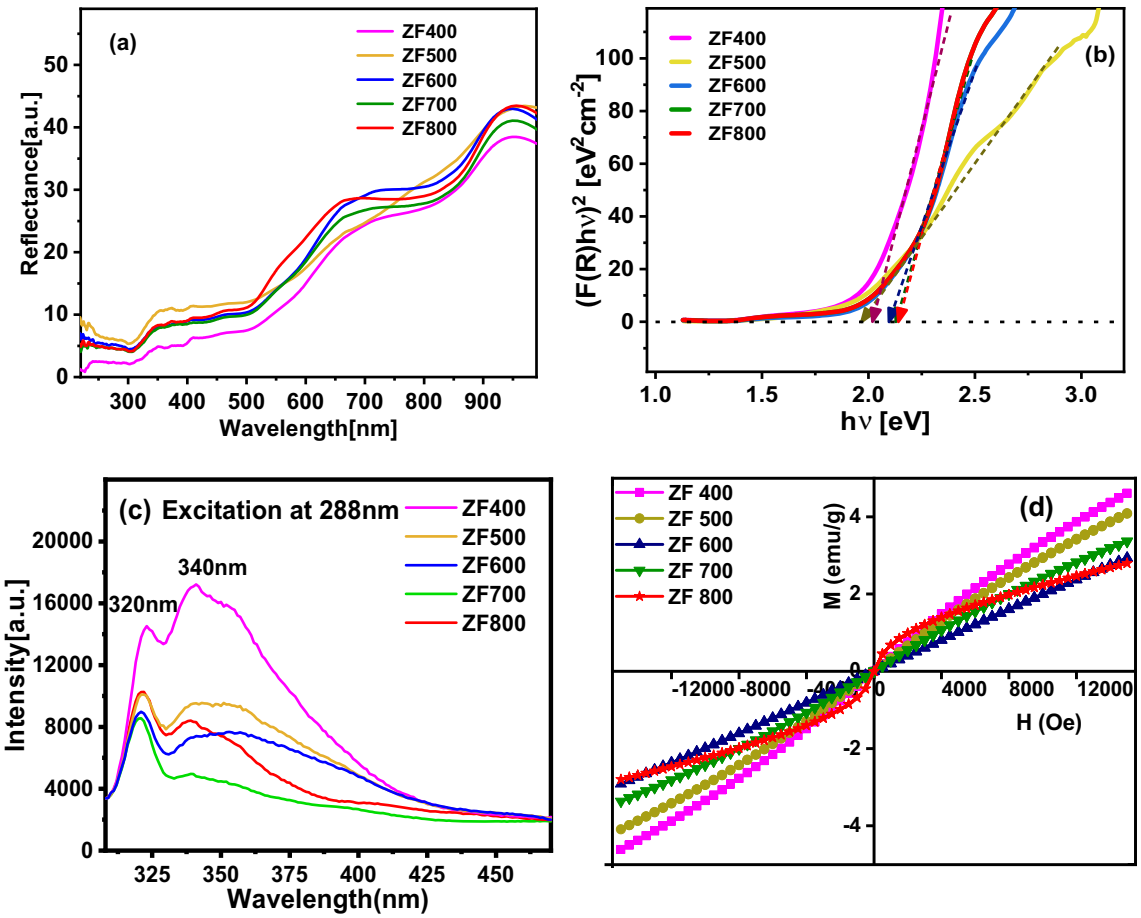

Figure 5. (**a**) Diffuse reflectance spectra and (**b**) Tauc plot of ZF400–ZF800 nanoparticles using UV–VIS DRS data. (**c**) Photoluminescence spectra of ZF400, ZF500, ZF600, ZF700 and ZF800 upon excitation at 288 nm. (**d**) M–H plot of ZF400, ZF500, ZF600, ZF700 and ZF800.

increased presence of Fe^{3+} in tetrahedrally coordinated sites caused a higher absorption (low reflectance) in the 1200 nm region [25].

The bandgap was evaluated by extrapolating the linear portion of the Tauc plot to $[F(R)h\upsilon]^2 = 0$ (figure 5b), where Kubelka–Munk function $F(R)$ for the powdered sample from UV–VIS DRS data is given by using equation (7) relating diffused reflectance (R), absorption (k) and scattering (s) coefficients.

$$F(R) = \frac{k}{s} = \frac{(1-R)^2}{2R}. \tag{7}$$

The direct bandgaps of ZF obtained ranged between 1.947 and 2.150 eV for the nanoparticles ZF500, ZF400, ZF700 and ZF800, which indicate a decrease in energy bandgap with the decrease in crystallite size (optical absorption redshift), presented in table 1. The decrease in energy bandgap as a function of grain size is less related to the quantum confinement effect and more to the presence of additional energy levels of subbands arising from surface/interface defects in bulk agglomerated particles as a result of calcination temperature [26].

The increase in calcination temperature would have increased the oxygen vacancies, which are sources of trapped exciton states that form a series of metastable energy levels within the energy gap, resulting in the redshift of the optical bandgap [27]. This explains the smaller bandgap (optical absorption redshift) shown by all the samples compared to the bulk value of zinc ferrite (2.3 eV) in contrast to the normal quantum confinement effects.

3.5 *Photoluminescence studies*

The photoluminescence (PL) emission of spinel ferrites is due to the charge transfer between the cation and its surrounding oxygen ions in tetrahedral and octahedral sites. The PL spectra for the synthesized samples upon excitation at 288 nm presented in figure 5c shows two emission peaks around 320 and 340 nm. The strong UV near-band edge emission at 320 nm could originate from the impurities or interstitial zinc defects. A broad band observed from 330 to 390 nm could be attributed to the broadening of the bandgap due to quantum confinement effects [28]. A clear

Table 2. Magnetization, M, thermal diffusivity, D, increase in D with respect to water and volume fraction for maximum D (V) in the presence of an external field of 1000 and 2000 Oe.

	External magnetic field of 1000 Oe				External magnetic field of 2000 Oe			
Sample	M (emu g^{-1})	$D \times 10^{-7}$ m^2s^{-1}	D_{ratio} with respect to base fluid	V (%)	M (emu g^{-1})	$D \times 10^{-7}$ m^2s^{-1}	D_{ratio} with respect to base fluid	V (%)
ZF600	0.20	1.16	0.8	2.9	0.40	4.01	2.9	2.7
ZF700	0.28	2.04	1.5	5.9	0.55	8.20	5.9	5.9
ZF500	0.33	3.66	2.6	2.9	0.66	4.14	3.0	2.2
ZF400	0.38	3.80	2.7	1.5	0.76	3.15	2.3	2.0
ZF800	0.67	4.97	3.6	5.8	0.98	2.79	2.0	5.0

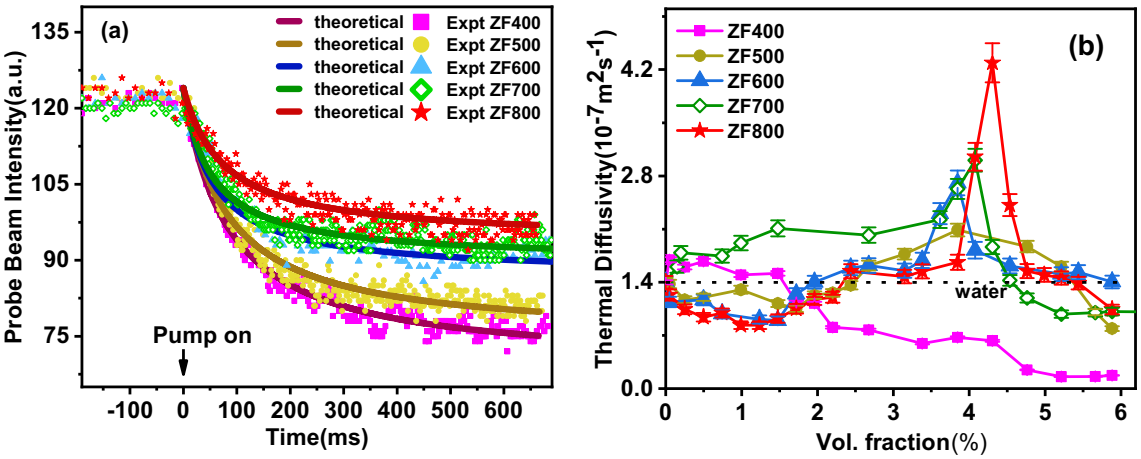

Figure 6. (**a**) Transient variation of probe intensity in the presence of a pump beam is fitted with theory. (**b**) Variation of thermal diffusivity with the volume fraction of ZF400, ZF500, ZF600, ZF700 and ZF800 in water.

decrease in intensity was noted for high-temperature calcined samples. In contrast to the other nanoparticle samples, the ZF700 sample showed quenching of PL intensity. This established the importance of the decay of excited charge carriers in a non-radiative manner, quicker charge transfer to the surface and delayed recombination, all of which can improve thermal diffusivity.

3.6 *Vibration sample magnetometer studies*

The magnetic ordering of the samples was evaluated using magnetization measurements and VSM studies. The normal spinel structure of bulk $ZnFe_2O_4$ has non-magnetic Zn ions occupying A-site alone. Hence, a weak antiferromagnetic exchange interactions in the B-site among magnetic Fe–Fe ions lead to a near-zero moment at room temperature. Contrary to this, the prepared samples show a ferrimagnetic nature (figure 5d), which can be attributed to the migration of cations between A and B sites that leads to a dominance of stronger Fe–Fe interaction between A–B sub-lattices over the Fe–Fe ions interaction in the B-site constituting an uncompensated moment.

The resulting magnetic moment can also emerge from $ZnFe_2O_4$ nanoparticles' spin canting, where some of the total spins at the surface will have a non-collinear arrangement with respect to the core spins because of broken exchange bonds and symmetry. Additionally, the M–H curve's non-saturation, even at the strongest applied field, suggests that spin disorder is present on the surface of $ZnFe_2O_4$. The core-shell model proposed a two-component nanoparticle system made up of ferrimagnetically aligned core spins and a surface layer resembling spin glass connected by exchange interactions to explain this behaviour. The magnetic moments in the core begin to align along the applied field as the field increases, and once alignment is complete, the saturation occurs in a typical Langevin-like manner. Only the surface layer of the particles is impacted by a further increase in the magnetic field. Even in very strong fields, the spin canting component from a significant fraction of particles on the surface of nanoparticles results in an unsaturated magnetization [29].

The S-shaped M–H curve of ZF800 sample indicates its superparamagnetic behaviour and single-domain formation. Table 2 presents the saturation magnetization M_s and remanent magnetization M_r of the samples. It was found that M_s decreased with an increase in calcination temperature, highlighting the relationship between cation migration-related inversion and crystallization as well as the presence of point defects like oxygen vacancies that interfere with the A–O–B super-exchange interaction between the magnetic cations in the two sub-lattices.

3.7 *Evaluation of thermal diffusivity*

Figure 6a shows the temporal probe beam intensity variation due to the thermal lens formation, evaluated using dual-beam thermal lens method, which was then fitted to obtain the thermal diffusivities of the samples as discussed in Section 2.4. The size and morphology of the dispersed magnetic particles, the magnetic dipolar interaction energy among the neighbouring magnetic nanoparticles, predominance of non-radiative decay, feasible heat transfer between the base fluid and nanoparticle, and crystallite size and morphology-dependent Brownian motion leading to convection of nanoparticles are some of the factors that are decisive in the thermal diffusivity of nanofluids [8,30].

Each nanoparticle in a magnetic nanofluid can be thought as having a magnetic moment of m. Equation (8) describes the interaction between ith and jth magnetic nanoparticles of moments $\overrightarrow{m_i}$ and $\overrightarrow{m_j}$, respectively, and $\overrightarrow{r_{ij}}$ as a function of their relative positions and orientations [31].

$$U_d(ij) = -3\left[\frac{(\overrightarrow{m_i}\,\overrightarrow{r_{ij}})(\overrightarrow{m_j}\,\overrightarrow{r_{ij}})}{r_{ij}^5} - \frac{\overrightarrow{m_i}\,\overrightarrow{m_j}}{r_{ij}^3}\right]; \overrightarrow{r_{ij}} = \overrightarrow{r_i} - \overrightarrow{r_j} \tag{8}$$

A measure of magnetic interaction energy between the contacting magnetic nanoparticles $U_d(ij)$ and the thermal energy k_BT is typically represented by a dimensionless parameter known as magnetic dipolar coupling constant $\lambda = [U_d(ij)/k_BT]$, where k_BT and T are the Boltzmann constant and absolute temperature, respectively. Thermal motion takes precedence over magnetic dipolar attraction in the absence of a magnetic field, which is represented as $\lambda < 1$. Due to this, the magnetic moments become randomly oriented, and Brownian motion of the nanoparticles takes control [4]. The energy of the magnetic interparticle interaction increases in the presence of an external magnetic field, counteracting the Brownian motion of the particles represented by $\lambda > 1$, and the magnetically momentous nanoparticles begin to align themselves in the direction of the magnetic field, making percolation effects the dominant mechanism. In order to investigate the effects of Brownian motion or percolation in tailoring the thermal diffusivity, the experiment was conducted in the absence and presence of a magnetic field, respectively.

3.7a *Thermal diffusivity in the absence of external field:* In the absence of an external magnetic field, the prepared magnetic nanofluids showed a 1.2- to 3.1-fold increase in thermal diffusivity compared to the base fluid, listed in table 2. The highest thermal diffusivity was shown by ZF800 and the least by ZF400 nanofluids. Thus, a linear dependence of the thermal diffusivity of the magnetic fluids on their calcination temperature was noted. In the limelight of Brownian motion and in the absence of a magnetic field, the particle size effects can be explained using equation (9) for Brownian velocity v [32], where ρ is the density and diameter of the nanoparticle.

$$v = \sqrt{\frac{18k_BT}{\pi\rho d^3}}. \tag{9}$$

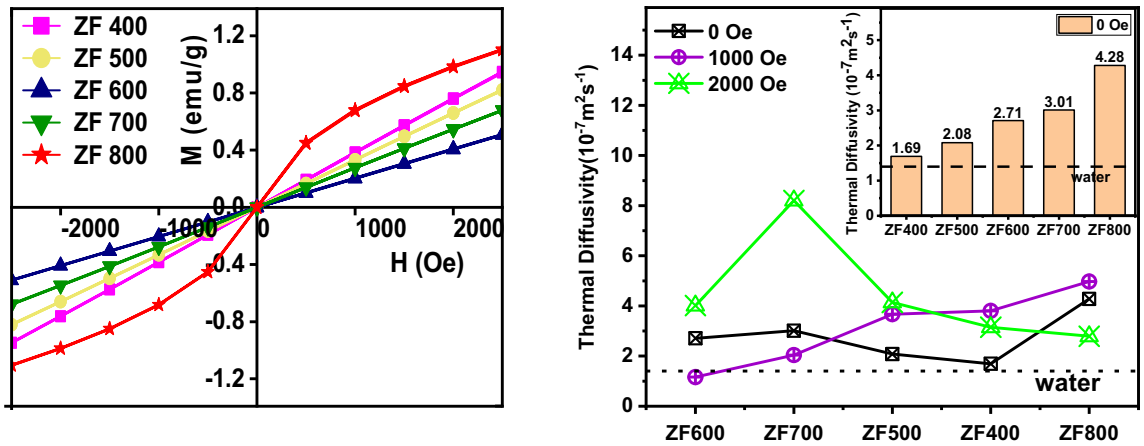

Figure 7. (**a**) M–H response of samples at 1000 and 2000 Oe. (**b**) Maximum thermal diffusivity of ZF600, ZF700, ZF500, ZF400 and ZF800 nanofluids in water, displayed in the increasing order of M–H response, at external magnetic fields of 0, 1000 and 2000 Oe. The inset shows the linear increase of thermal diffusivity with samples ZF400 to ZF800 shown in the increasing order of crystallite size.

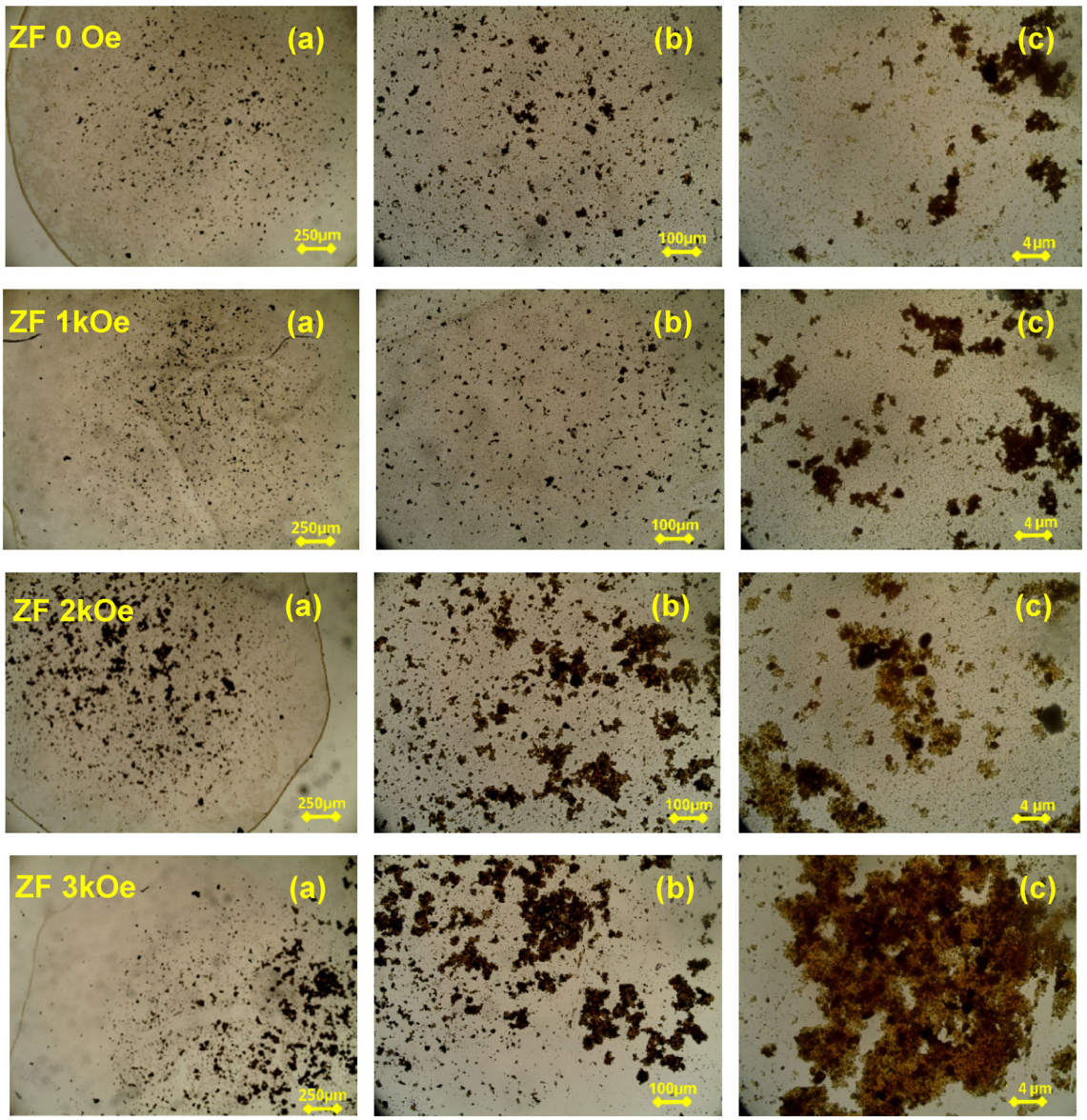

Figure 8. Optical microscope images of the ZF700 film dried in the presence of magnetic field of 0 Oe, 1 kOe, 2 kOe and 3 kOe at (**a**) 40×, (**b**)100× and (**c**) 400× magnifications.

Despite having a larger particle size for high-temperature calcined samples, the faster heat dissipation of these samples can be attributed to a better magnetic coupling among the neighbouring nanoparticles favouring uniform distribution and channeling better diffusivity. The PL spectra also supported an increase in thermal diffusivity for high-temperature calcined samples as they showed quenching of radiative emission and hence favoured the non-radiative decay required for thermal lens formation. Nevertheless, at volume fractions of less than 2.5%, ZF800 showed the least thermal diffusivity, shown in figure 6b, which may be due to the less magnetic coupling at these volume fractions and hence the particle size effects decided the poor convection via Brownian motion. A uniform distribution of particles may have facilitated better thermal diffusivity over larger ranges of volume fraction of ZF700. Thermal diffusivity lower than the base fluid was noticed for ZF400 beyond 2% of volume fraction which could be due to the hindrance of heat transfer by its amorphous nature. As the concentration increased, agglomeration of magnetic nanoparticles would have disrupted the Brownian motion of the particles and increased the interfacial thermal resistance between the fluid and the nanoparticles.

3.7b *Thermal diffusivity in the presence of external field*: Further investigation was done in the presence of an external magnetic field in the range of 1 and 2 kOe. Thermal diffusivity of the nanofluids seemed to increase for

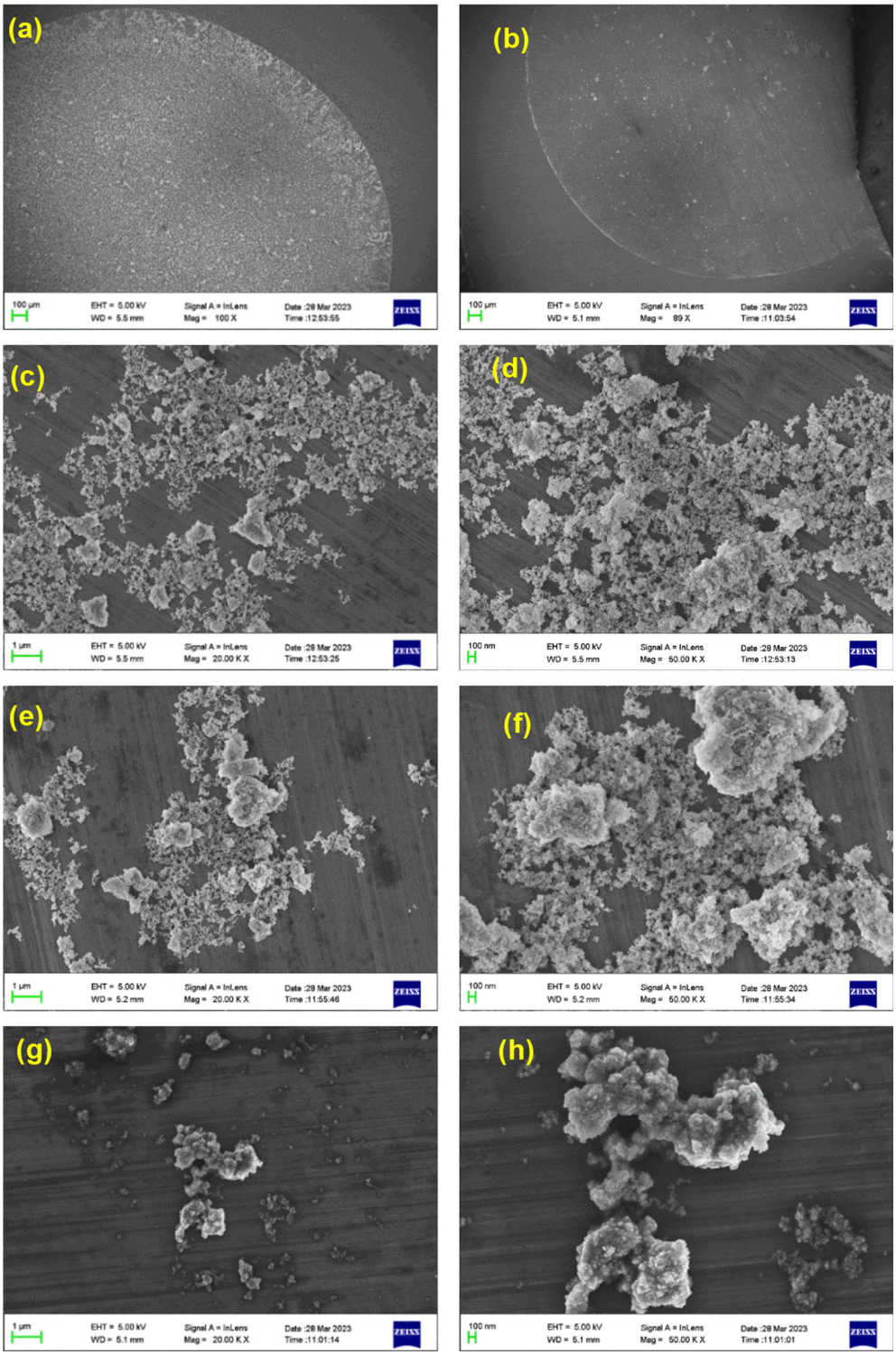

Figure 9. FESEM images of the film dried at (**a**) 0 kOe and (**b**) 2 kOe at 100 μm scale. FESEM images of the central portion of the film dried with (**c**, **d**) 0 Oe, (**e**, **f**) 1 kOe, (**g**, **h**) 2 kOe at 1 μm and 100 nm scale, respectively.

ZF400, ZF500, and ZF800 at 1000 Oe compared to that in no applied field, shown in table 2. This could be explained as the alignment of dispersed magnetic nanoparticles to form uniform chains due to their higher magnetic susceptibility and dependence of magnetic interaction on their volume fraction. While the ZF600 and ZF700 were the less susceptible samples and hence proper alignment could not have happened to facilitate easier thermal diffusivity.

Thus, a linear dependence of thermal diffusivity on the magnetic susceptibility of the dispersed magnetic nanoparticles was noted in 1 kOe, shown in figure 7.

The case reversed when the magnetic field was increased to 2 kOe, in which ZF700 showed the highest thermal diffusivity of 8.2 $\times 10^{-7} m^2 s^{-1}$ (6-fold increase) at a volume fraction of 5.9% followed by ZF500 and ZF600. Philip *et al* [33] have also reported the formation of chain-like structures serving as bridge for transportation of thermal energy and an enhancement of thermal conductivity of 300% (4-fold) beyond the Maxwell limit was obtained at a particle loading of 6.3%.

The least thermal diffusivity was shown by the most magnetic susceptible sample ZF800 at 2 kOe. This could be explained due to the chain zippering reported in the literature at high magnetic fields hindering the smooth diffusivity of the heat in magnetic nanofluids [34]. The value of thermal diffusivity for ZF700 was also checked at 3 kOe and showed a decrease in thermal diffusivity to 2.45 $\times 10^{-7} m^2 s^{-1}$ which is lesser than that at no field case and substantiates the claim of chain zippering at high fields.

3.7c *Optical and FESEM imaging of magnetic nanofluids*: To analyse the nature of clustering of particles in the presence of magnetic field, the colloidal solution of ZF700 was dried in the presence of external magnetic field. The prepared films were then analysed under optical microscope and FESEM and the images are shown in figures 8 and 9, respectively. The images substantiate the idea of clustering of nanoparticles in the presence of magnetic field and corresponding interaction to facilitate better thermal diffusivity. At zero applied field, there was random clustering depending on the random aggregation of the particles. As the field was increased to 1 kOe, an ordered clustering was visible which aggravated with further application of fields. Thus, percolation effects were dominant over the Brownian motion in deciding the thermal diffusivity offered by the magnetic nanofluids.

Thus size, morphology, volume fraction and magnetic susceptibility of the dispersed magnetic nanoparticles are instrumental in deciding the magnetic field at which the maximum thermal diffusivity can be obtained. Therefore the work offers a promising application for developing nanofluids with magnetically tunable thermal diffusivity.

4. Conclusion

The structural, morphological and magnetic analysis of synthesized nanoparticles using XRD, FESEM, FTIR and VSM confirmed the characteristics of zinc ferrite nanoparticles used to form magnetic nanofluids in water. The evaluation of optical features via UV–VIS DRS and PL spectra revealed a red-shifted bandgap and a quenched emission suitable for non-radiative decay, one of the prerequisites for faster thermal decay in a heat transfer nanofluid. The work demonstrated how customizing the characteristics of the nanoparticles for achieving increased thermal diffusivities depended on the calcination temperature during synthesis, the volume fraction of dispersed magnetic particles in the base fluid, and the applied magnetic field. Better magnetic coupling, uniform particle distribution, high crystallinity and increased magnetic susceptibility of the dispersed nanoparticles have facilitated the formation of chain-like structures enabling the percolation effects as a dominant means of enhancing the thermal diffusivity of the fluid. The work reports for the first time a 6-fold enhancement in thermal diffusivity than that of base fluid water in the presence of magnetic field. Thus the work revealed the tunability of heat transfer characteristics of zinc ferrite nanofluids in water with calcination temperature, volume fraction of dispersed particles and the applied magnetic field.

Acknowledgements

We wish to acknowledge DST FIST for supporting the Department of Physics, St. Teresa's College (Autonomous), Ernakulam. We also acknowledge the service by SAIF IIT Madras, Department of Physics CUSAT, STIC CUSAT and Department of Botany, St. Teresa's College for the characterization of the samples.

References

[1] Keblinski P, Eastman J A and Cahill D G 2005 *Mater. Today* **8** 36
[2] Ganvir R B, Walke P V and Kriplani V M 2017 *Renew. Sustain. Energy Rev.* **75** 451
[3] Masuda H, Ebata A, Teramae K and Hishinuma N 1993 *Netsu Bussei* **7** 227
[4] Nkurikiyimfura I, Yanmin Wang, Zhidong Pan and Dawei Hu 2011 *Int. Conf. Mater. Renew. Energy Environ.*, Shanghai, China: IEEE p 1333–7
[5] Yang L, Ji W, Mao M and Huang J 2020 *J. Clean. Prod.* **257** 120408
[6] Pankhurst Q A, Connolly J, Jones S K and Dobson J 2003 *J. Phys. Appl. Phys.* **36** R167
[7] Shima P D, Philip J and Raj B 2009 *Appl. Phys. Lett.* **95** 133112
[8] Abareshi M, Goharshadi E K, Mojtaba Zebarjad S, Khandan Fadafan H and Youssefi A 2010 *J. Magn. Magn. Mater.* **322** 3895
[9] Qin M, Shuai Q, Wu G, Zheng B, Wang Z and Wu H 2017 *Mater. Sci. Eng. B* **224** 125
[10] Kmita A, Pribulova A, Holtzer M, Futas P and Roczniak A 2016 *Arch. Metall. Mater.* **61** 2141
[11] Saravanan M and Girisun T C S 2017 *Appl. Surf. Sci.* **392** 904
[12] Jogi J K, Singhal S K, Jangir R, Dwivedi A, Tanna A R, Singh R *et al* 2022 *J. Electron. Mater.* **51** 5482
[13] Haghshenas F, Talaie M and Nasr S 2011 *Therm. Sci.* **15** 183

[14] Francis F, Anila E I and Joseph S A 2020 *Optik* **219** 165210
[15] Mathew S, Francis F, Joseph S A and M.S. K, 2021 *Nano-Struct. Nano-Objects* **28** 100784
[16] Gupta M, Singh V and Said Z 2020 *Sustain. Energy Technol. Assess.* **39** 100720
[17] Syam Sundar L, Naik M T, Sharma K V, Singh M K and Siva Reddy TCh 2012 *Exp. Therm. Fluid Sci.* **37** 65
[18] Pius M, Francis F and Joseph S 2023 *J. Nano Res.* **78** 59
[19] Kurian A, George N A, Paul B, Nampoori V P N and Vallabhan C P G 2002 *Laser Chem.* **20** 99
[20] Ani Joseph S, Mathew S, Sharma G, Hari M, Kurian A, Radhakrishnan P *et al* 2010 *Plasmonics* **5** 63
[21] Punnakkal V S, Francis F, Pius M, Santhi A and Anila E I 2023 *Mater. Today Commun.* **34** 105151
[22] Patterson A L 1939 *Phys. Rev.* **56** 978
[23] Wongyara C, Harnkar P, Suwanchawalit C, Puangpetch T, Laohhasurayotin K and Patil A 2017 *Key Eng. Mater.* **757** 125
[24] Pradeep A, Priyadharsini P and Chandrasekaran G 2011 *J. Alloys Compd.* **509** 3917
[25] Granone L I, Ulpe A C, Robben L, Klimke S, Jahns M, Renz F *et al* 2018 *Phys. Chem. Chem. Phys.* **20** 28267
[26] Kislov N, Srinivasan S S, Emirov Yu and Stefanakos E K 2008 Mater. *Sci. Eng. B* **153** 70
[27] Chakraborty M, Thangavel R, Biswas A and Udayabhanu G 2016 *CrystEngComm* **18** 3095
[28] Harzali H, Marzouki A, Saida F, Megriche A and Mgaidi A 2018 *J. Magn. Magn. Mater.* **460** 89
[29] Kodama R H, Berkowitz A E, McNiff E J Jr and Foner S 1996 *Phys. Rev. Lett.* **77** 394
[30] Eapen J, Williams W C, Buongiorno J, Hu L, Yip S, Rusconi R *et al* 2007 *Phys. Rev. Lett.* **99** 095901
[31] Ivanov A O, Kantorovich S S, Mendelev V S and Pyanzina E S 2006 *J. Magn. Magn. Mater.* **300** e206
[32] Prasher R, Phelan P E and Bhattacharya P 2006 *Nano Lett.* **6** 1529
[33] Philip J, Shima P D and Raj B 2007 *Appl. Phys. Lett.* **91** 203108
[34] Philip J, Shima P D and Raj B 2008 *Nanotechnology* **19** 305706